AD-A033 484 DAVID W TAYLOR NAVAL SHIP RESEARCH AND DEVELOPMENT CE--ETC F/G 11/6
DETERMINATION OF PREFRACTURE FATIGUE DAMAGE.(U)
NOV 76 I R KRAMER

UNCLASSIFIED MAT-76-74 NL

1 OF 1
AD
A033484

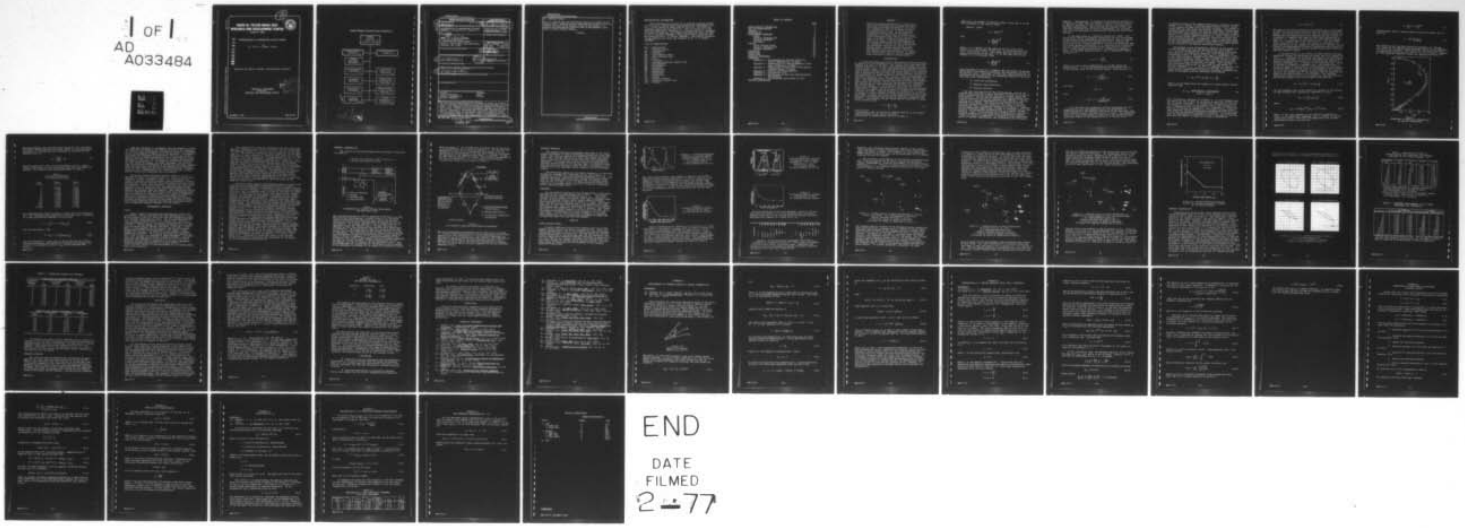

END

DATE
FILMED
2-77

MAT-76-74

DAVID W. TAYLOR NAVAL SHIP RESEARCH AND DEVELOPMENT CENTER

Bethesda, Md. 20084

ADA033484

DETERMINATION OF PREFRACTURE FATIGUE DAMAGE

by
Dr. Irvin R. Kramer, Editor

Approved for public release; distribution unlimited

MATERIALS DEPARTMENT
Annapolis
RESEARCH AND DEVELOPMENT REPORT

November 1976

MAT-76-74

Determination of Prefracture Fatigue Damage

MAJOR DTNSRDC ORGANIZATIONAL COMPONENTS

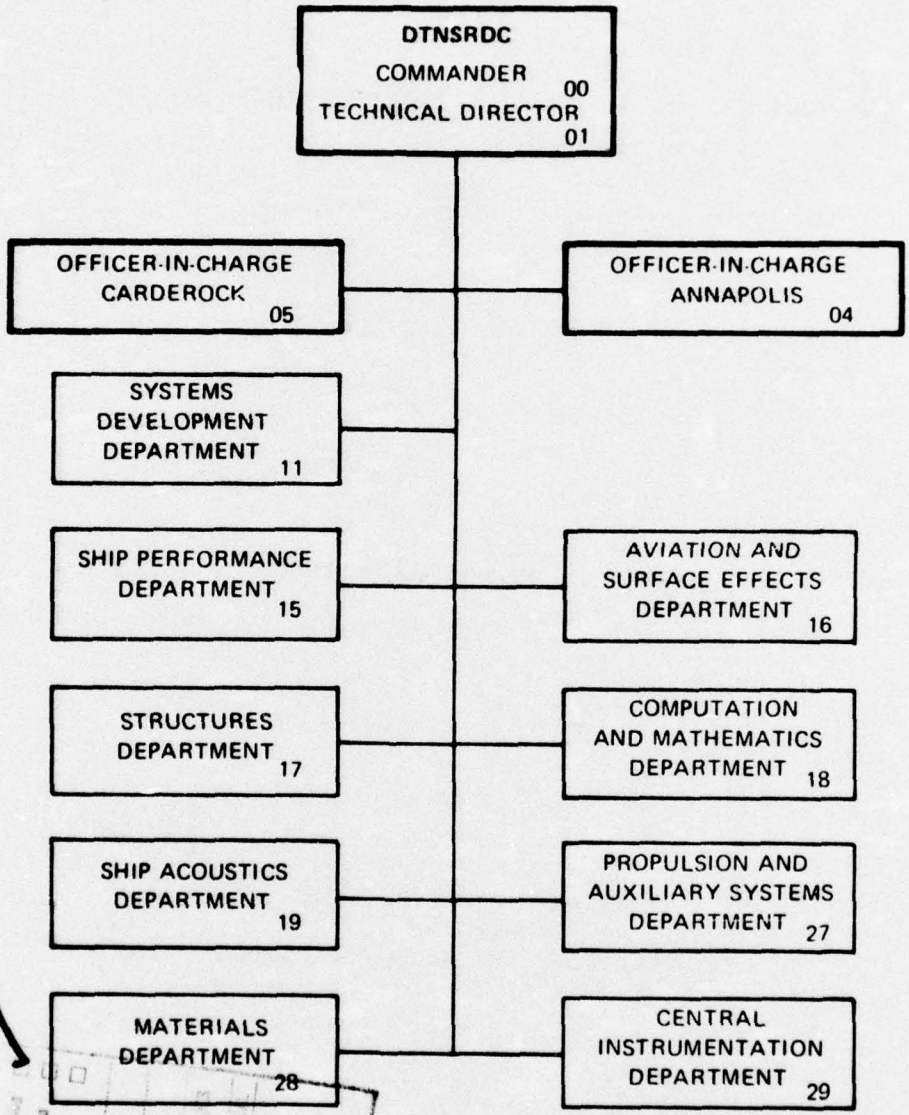

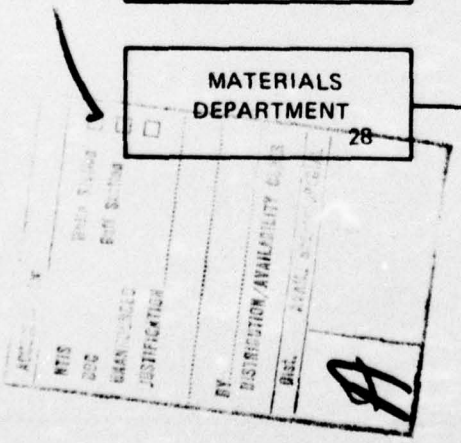

UNCLASSIFIED

SECURITY CLASSIFICATION OF THIS PAGE (When Data Entered)

REPORT DOCUMENTATION PAGE

READ INSTRUCTIONS BEFORE COMPLETING FORM

1. REPORT NUMBER: MAT-76-74	2. GOVT ACCESSION NO.
3. RECIPIENT'S CATALOG NUMBER: Interim rept.	
4. TITLE (and Subtitle): DETERMINATION OF PREFRACTURE FATIGUE DAMAGE.	5. TYPE OF REPORT & PERIOD COVERED: Research and Development, Interim
	6. PERFORMING ORG. REPORT NUMBER
7. AUTHOR(s): Irvin R. Kramer, Editor	8. CONTRACT OR GRANT NUMBER(s)
9. PERFORMING ORGANIZATION NAME AND ADDRESS: David W. Taylor Naval Ship R&D Center, Bethesda, MD 20084	10. PROGRAM ELEMENT, PROJECT, TASK AREA & WORK UNIT NUMBERS: Project Element 61152N; Task Area ZR 022-0101; Work Unit 2802-001
11. CONTROLLING OFFICE NAME AND ADDRESS	12. REPORT DATE: November 1976
	13. NUMBER OF PAGES: 44
14. MONITORING AGENCY NAME & ADDRESS (if different from Controlling Office): ZR022 01	15. SECURITY CLASS. (of this report): Unclassified
	15a. DECLASSIFICATION/DOWNGRADING SCHEDULE

16. DISTRIBUTION STATEMENT (of this Report)

Approved for public release; distribution unlimited

17. ZR022010 1

17. DISTRIBUTION STATEMENT (of the abstract entered in Block 20, if different from Report)

18. SUPPLEMENTARY NOTES

19. KEY WORDS (Continue on reverse side if necessary and identify by block number)

Fatigue
X-ray diffraction
Magnetic permeability
Acoustic emission
Aluminum
Steel
Silicon

20. ABSTRACT (Continue on reverse side if necessary and identify by block number)

The dislocation distribution as a function of depth was investigated on fatigued and unidirectionally strained specimens of 4130 steel, 2024 aluminum as well as on single crystals of aluminum and silicon. Using X-ray line broadening together with the Berg-Barrett technique it was shown that the excess dislocation density was much larger in the surface layer to a depth of about 100 micrometres than in the bulk. From the measurements of the initial permeability at high frequencies (10 kilohertz) it would

DD FORM 1 JAN 73 1473 EDITION OF 1 NOV 65 IS OBSOLETE
S/N 0102-014-6601

UNCLASSIFIED
SECURITY CLASSIFICATION OF THIS PAGE (When Data Entered)

408635

20. Abstract (Cont)

also be inferred that the dislocation density was larger in the surface layer. Because acoustic emissions were found at very low stresses relative to the maximum stress during fatigue, it appears that this method cannot be used on ferromagnetic materials to detect fatigue damage.

(Author)

ADMINISTRATIVE INFORMATION

This investigation is part of an in-house research program at the David W. Taylor Naval Ship Research and Development Center. It was conducted under task ZR 022-0101. The work was performed under work unit 2802-001. The X-ray,portion of the work was conducted by Professor S. Weissmann and Mr. R. Pangborn of Rutgers University. The magnetic permeability work was done by Dr. S. Friedman (DTNSRDC), while the acoustic emission work was conducted by Dr. J. Faller (DTNSRDC). The overall direction of the research was under the guidance of Dr. I. R. Kramer (DTNSRDC).

LIST OF ABBREVIATIONS

B-B - Berg-Barrett
° C - degrees Celsius
cm - centimetres
db - decibels
emf - electromotive force
fcc - face centered cubic
Hz - hertz
kHz - kilohertz
ksi - thousand pounds per square inch
mA - milliamperes
mH - millihenries
MHz - megahertz
mm - millimetres
MPa - megapascals
mv - millivolts
μm - micrometres
No. - number
o.d. - outside diameter
psi - pounds per square inch
sec - seconds

TABLE OF CONTENTS

	Page
ADMINISTRATIVE INFORMATION	i
LIST OF ABBREVIATIONS	i
ABSTRACT	1
INTRODUCTION	1
EXPERIMENTAL PROCEDURE	8
X-Ray	8
Magnetic Permeability	10
Acoustic Emission	12
Specimens	12
RESULTS	12
X-Ray Rocking Curves	12
Magnetic Permeability	18
Acoustic Emission	21
DISCUSSION	22
CONCLUSIONS	24
FUTURE WORK	24
TECHNICAL REFERENCES	25
APPENDIXES	
Appendix A - Relationship of Internal Stress to Initial Permeability (3 pages)	
Appendix B - Penetration of a Varying Magnetic Field into a Conductor (4 pages)	
Appendix C - Computation of Phase from an Elliptical Lissajou Figure (2 pages)	
Appendix D - Trace of B/H Characteristic	
Appendix E - Calculation of f_g	
Appendix F - Calculation of $\Delta\mu/\mu$ from High-Frequency Measurements	
Appendix G - Low Frequency Calculation of $\Delta\mu/\mu$	
INITIAL DISTRIBUTION	

ABSTRACT

The dislocation distribution as a function of depth was investigated on fatigued and unidirectionally strained specimens of 4130 steel, 2024 aluminum as well as on single crystals of aluminum and silicon. Using X-ray line broadening together with the Berg-Barrett technique it was shown that the excess dislocation density was much larger in the surface layer to a depth of about 100 micrometres than in the bulk. From the measurements of the initial permeability at high frequencies (10 kilohertz) it would also be inferred that the dislocation density was larger in the surface layer. Because acoustic emissions were found at very low stresses relative to the maximum stress during fatigue, it appears that this method cannot be used on ferromagnetic materials to detect fatigue damage.

INTRODUCTION

It has been shown previously[1] that during uniaxial fatiguing of metals the work hardening of the surface layer increases more rapidly than that in the bulk. For high-cycle fatigue after the first 1/2 cycle (R = 1)* the work hardening was confined entirely to the surface layer. From a systematic investigation[2] on aluminum 2014-T6, titanium (6 Al/4V) and a 4130 steel it was observed that a propagating fatigue crack was formed whenever the surface work hardening, as characterized by the surface layer stress, τ_s* reached a critical value. This critical value was independent of the stress amplitude, prior fatigue stress history, and environment. These parameters affected the rate of surface work hardening but not the critical value for the fatigue crack formation. The observation on crack formation led directly to a mechanism for fatigue damage. It was proposed[2] that since the surface layer acted to oppose the motion of dislocations it could provide a barrier to support a piled up array or accumulation of dislocations of like sign. When the barrier is of sufficient strength to support a critical number of these dislocations, fracture will occur when, locally, the stress fields associated with the accumulation of the dislocations exceed the fracture strength of the material. Accordingly, fatigue damage may be described in terms of the surface layer

$$f_\ell \equiv \frac{N}{N_o} = \frac{\tau_s}{\tau_s^*} \qquad (1)$$

---

[1] Superscripts refer to similarly numbered entries in the Technical References at the end of the text.

*Definitions of abbreviations used are on page i.

where N_o is the number of cycles to form a crack and τ_s is the work hardening of the surface layer.

However, since[3]

$$\tau_s = \alpha b G \rho_s^{1/2} \tag{2}$$

then

$$f_\ell = \left(\frac{\rho_s}{\rho_s^*}\right)^{1/2} \tag{3}$$

where α is a constant of the order of 1/5, G is the shear modulus, b is the burgers vector and ρ is the dislocation density. Since Taira, et al,[4] have shown that the ratio of the excess dislocation of one sign , D, to the total dislocation density, ρ, is a constant, then

$$f_\ell = \left(\frac{D_s}{D_s^*}\right)^{1/2} \tag{4}$$

From equations (3) and (4) it appears that the extent of fatigue damage may be determined by measuring the dislocation density in the surface layer. Therefore, to this end, three methods for the nondestructive evaluation of the dislocation density in the surface layer were investigated:

- X-ray line broadening.
- Magnetic characteristics.
- Acoustic emission.

For the X-ray portion of this investigation, silicon and aluminum were selected as model materials to study the effect of plastic deformation and fatigue cycling on surface layers and bulk material. Silicon may be regarded as a representative of a class of materials having low stacking fault energy,[5-9] whereas aluminum is a typical representative of materials with high stacking fault energy. The stress-strain curves of silicon and other diamond structure materials, when taken at elevated temperatures, show a pronounced analogy to fcc metals.[9] However, at low deformation temperatures, silicon is extremely brittle and exhibits the deformation characteristics of a typical ceramic material. Thus, if dislocations are introduced into crystals at elevated temperatures, the dislocation configuration remains "frozen-in" when the temperature is lowered to room temperature since, at ambient temperatures, the dislocations are virtually

immobile. Consequently, in studying the deformation response as a function of depth from the surface, removal of surface layers by chemical polishing is not likely to disturb the induced dislocation configuration. While silicon and aluminum single crystals were subjected only to tensile deformation, the aluminum 2024 alloy was subjected to both tensile deformation and fatigue cycling.

It has been shown in a detailed theoretical study[10] that dislocations affect the magnetic properties via the interactions of the stress field surrounding the dislocation with the magnetoelastic forces within each crystalline grain. Although the derivation of the various equations[10] is strictly applicable only at or near magnetic saturation, it is indicated that dislocation strains affected other portions of the magnetization curve as well. A more simplified derivation[11] reproduced in appendix A shows that whenever magnetization is due to independent domain rotation then

$$\mu_o - 1 = \frac{I_s^2}{\lambda_s \tau_i} \tag{5}$$

where μ_o is the initial permeability, I_s is the saturation mangetization, λ_s is the magnetostrictive coefficient, and τ_i is the average value of the internal stress. From equation (2)

$$\mu_o - 1 = \frac{I_s^2}{\lambda_s \alpha b G \rho_s^{1/2}} \tag{6a}$$

and since

$$\rho/D = C \tag{6b}$$

then

$$\mu_o - 1 = \frac{I_s^2}{\lambda_s \alpha b C G D_s^{1/2}} \tag{6c}$$

Over and above the parameters usually associated with the magnetization of a ferromagnetic metal, the phenomenon of Barkhausen noise[12] has recently been found to be associated with both residual stress[13] and grain size[14] in steel. The Barkhausen effect has been established as being due to the relatively discontinuous nature of the mangetization of a ferrous metal.[12-15]

In certain regions of the magnetization curve, favorably oriented domains (i.e., regions of uniform magnetization) grow in volume at the expense of those least favorably oriented. This growth in volume does not take place continuously (assuming a continuously changing magnetizing field) but executes many small, rapid jumps. The resultant flux changes will generate many transient, voltage spikes in a suitably disposed pickup coil. Hence, observation of these voltage spikes should yield some indication of grain size and dislocation density. In summation, there is plentiful theoretical and experimental evidence that suggests that measurement of the ferromagnetic properties of steel near the surface should yield a measure of the surface dislocation density.

Measurement of any ferromagnetic property at the surface of a steel specimen must take due account of the "skin effect," i.e., the lack of penetration of a varying magnetic field below the surface of an electrical conductor. This propensity for time-varying fields to decrease with depth in conductors is due to the "eddy currents" created by the electromotive force induced by the varying magnetic fields. These currents create a secondary magnetic field that interacts with the primary field and causes the net field to decrease with depth. The treatments of this phenomenon most suited to the needs at hand appear in several treatises.[15] [16] [17] As shown in appendix B, starting with the basic Maxwell field equations, we find that the magnetic field inside a planar and a cylindrical conductor decreases with depth in accordance with the following relationships

$$H = H_o \, \epsilon^{-x/s} \cos\left(2\pi \, ft - \frac{x}{s}\right) \tag{7}$$

where x is the depth below the surface of a semi-infinite planar conductor and,

$$H = H_o \, \frac{ber^2(2\theta r/d) + bei^2(2\theta r/d)}{ber^2 \, \theta + bei^2 \, \theta} \tag{8}$$

For a cylindrical conductor of diameter d, r is the distance from the center of the cylinder to the point in question, and ber and bei are Bessel functions. In either case, the magnetic field at the surface is parallel to the surface and to the cylinder axis and is assumed to vary sinusoidally at a frequency f. Other symbols are as defined in appendix B. The planar solution yields some important, easily interpretable consequences that carry over to the less interpretable cylindrical solution. It can be shown that the magnitude of H decreases to 1/e of its value at the surface when the depth x is equal to s which is defined by

$$s = (\pi\mu\sigma f)^{-1/2} \tag{9}$$

The phase of the field referred to the surface shi ts with depth so that at one skin depth the field lags the surface field by 1 radian. The implication of this is that the effective depth for determining the electromotive force produced by flux changes in a specimen is somewhat less than the skin depth determined by equation (9). Finally, for materials of given magnetic properties, i.e., permeability μ and conductivity σ, the skin depth varies inversely as $\sqrt{f}$. Hence, the higher the frequency, the more indicative is the response to the value of μ and of σ at the surface, and measurements at several frequencies should yield an indication of differences between volume and surface microstructure and residual stress.

A detailed theory of the effects of eddy currents has been worked out largely in connection with their use as an inspection tool.[16,17] Confining our attention initially to the geometry of cylindrical specimens, we find that the effects of eddy currents are most conveniently expressed by introducing the concept of effective permeability. It enters in the following way: assume a cylinder of diameter d, permeability μ, and conductivity σ. If the cylinder is surrounded by a time-periodic but spatially unvarying magnetic field H, then the electromotive force induced in a coil of n turns of diameter d_c will depend on the applied field H, the permeability of the cylinder, and the magnitude and phase of the eddy currents in the cylinder. The resultant electromotive force will be out of phase with the applied field and in very general terms can be shown to be given by

$$E_r = E_o \left(1-\eta + \eta\mu\mu_{eff.r}\right) \tag{10a}$$

for the component that would normally be present in the absence of eddy currents and a quadrature component E_i, where

$$E_i = E_o \left(\eta\mu\mu_{eff.i}\right) \tag{10b}$$

where

$$E_o = 2\pi fn\left(\pi {d_c}^{2/4}\right) H_o \times 10^{-8} \text{ volts} \tag{10c}$$

$\mu_{eff.r}$ is the real component of the effective permeability, $\mu_{eff.i}$ is the immaginary component, and $\eta = (d/do)^2$ is the so-called fill factor. Note that the magnitude of the induced electromotive force E is given by

$$E = \left(E_r^2 + E_i^2\right)^{1/2} \tag{11}$$

and the phase angle φ between applied field and induced emf is given by

$$\varphi = \tan^{-1}\left(E_i / E_r\right) \tag{12}$$

The formalism that has been stated by equations (10) through (12) takes on real meaning when numerical values of the components of η_{eff} can be assigned. These have been calculated from basic considerations arising out of equation (3) as outlined in appendix B. The resultant numerical values are embodied in figure 1.[17]

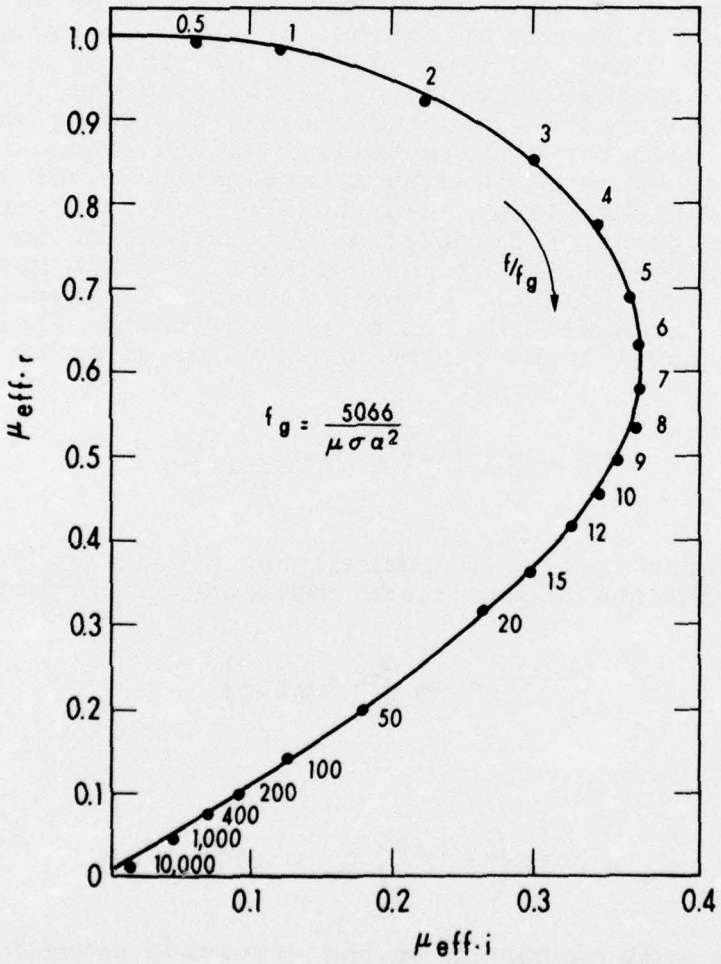

Figure 1
Components of Effective Permeability
of Various Frequencies

The key parameters for entering these curves are the fill factor previously defined and the f/f_g ratio, where f is the frequency of H and f_g is a characteristic frequency of the material and geometry given by

$$f_g = \frac{5066}{\mu\sigma d^2} \quad \text{Hz} \tag{13}$$

where the units of σ and d are metres/ohm-mm and cm, respectively.[16] The values of μ_{eff} for various f/f_g have also been tabulated,[16] the results being reproduced herein in table 1.

TABLE 1
Effective Permeability
as a Function of f/f_g

f/f_g	$\mu_{eff.r}$	$\mu_{eff.i}$
0	1.000	0.000
1	0.9798	0.1216
2	0. 264	0.2234
5	0.6992	0.3689
10	0.4678	0.3494
20	0.3180	0.2657
50	0.2007	0.1795
100	0.1416	0.1313
200	0.1001	0.0950
400	0.0707	0.0682
1000	0.0447	0.0437
10,000	0.0141	0.0140

For considerations closely related to those that lead to equation (10), the inductance and resistance of a helical coil, concentric to a long, cylindrical specimen, are given by[17]

$$L = L_o \left(1 - \eta + \eta\mu\mu_{eff.r}\right) \tag{14a}$$

for the inductance L, and

$$R - R_o = \omega L_o \left(\eta\mu\mu_{eff.1}\right) \tag{14b}$$

for the resistance R. Note that L_o and R_o are the coil inductance and resistance when devoid of a cylindrical specimen, and $\omega = 2\pi f$. The requires values of μ_{eff} may be obtained from figure 1.

From the foregoing it is apparent that measurement of either the amplitude and phase of the induced voltage or the impedance of a helical coil surrounding a cylindrical specimen is dependent on the electromagnetic properties of the specimen. Furthermore, the higher the frequency of measurement, the more the results should depend on surface properties, since both magnetic fields and eddy currents fall off with depth in a manner approximately according to equation (9). Although the theoretical equations for skin depth are simpler for planar specimens, the relative ease of controlled measurements on cylindrical specimens suggests their use initially. As for the other parameters of interest, coercive force, Rayleigh constant, and Barkausen noise, measurements were not accomplished in this reporting period, so that further theoretical discussion will be deferred.

The possibility of detecting fatigue damage by acoustic emission is based on the Kaiser effect.[18] Kaiser reported when specimens of steel, aluminum, copper, pine and boxwood were loaded in tension, and then unloaded, upon reloading no acoustic emission activity was detected until the previous maximum stress was exceeded. Later, Duke and Kline[19] reported that prestressed specimens of 70-30 brass and 1100 aluminum exhibited acoustic emission bursts at stresses below the previous maximum stress whenever the surface layer was removed. This observation coupled with the observation that the surface layer work hardened more than the interior in fatigue as well as in uniaxial deformation led to the idea that a measure of fatigue damage could be obtained by determining the increase in the acoustic emission threshold stress as a function of the number of fatigue cycles. This concept appeared feasible provided other emission sources, such as growth of magnetic domains, did not operate.

EXPERIMENTAL PROCEDURE

X-RAY

Single crystals of silicon and aluminum were sliced into thin wafers. Tensile specimens with gage dimensions of 5 x 1.5 mm and lengths 20 mm (Si) and 15 mm (Al) were prepared by means of a Servomet spark-erosion cutter. The silicon specimens had (112) surface orientation and [110] tensile axis, while the aluminum specimens had (100) surface orientation and [100] tensile axis. Surface damage was removed by lapping with 600-grit silicon carbide and by chemical polishing (1 part HF, 3 parts HNO_3, 2 parts CH_3COOH) for the silicon, and by spark-erosion planing followed by electropolishing (1 part HNO_3, 3 parts CH_3COOH for aluminum). At least 70 μm was removed to obtain damage-free surfaces. The aluminum specimens were annealed at 600° C for 20 hours in a protective argon atmosphere. All specimens were deformed on an Instron universal tester. Silicon specimens were deformed at a strain rate of 5.9×10^{-5} sec^{-1} above the ductile-brittle temperature in an argon atmosphere. Aluminum specimens were tested at a strain rate of 3.3×10^{-3} sec^{-1} below 0° C and maintained at 0° C during subsequent X-ray analysis.

The aluminum 2024 alloy was obtained as bar stock with composition (weight percent) 3.99 Cu, 1.35 Mg, 0.50 Mn, and principal impurity content of 0.29 Fe, 0.10 Si, 0.08 Zn, 0.02 Ti, and 0.02 Cr. The stock was fabricated into cylindrical fatigue specimens with a gage diameter of 3 mm and a gage length of 6.35 mm. Specimens were heat treated in a tilting furnace at 495°±5° C for 2 hours in an argon atmosphere, quenched in ice water at 0° C, and aged at ambient temperatures for 48 hours. After heat treatment the specimens were polished mechanically with polishing alumina, using 0.05-μm particles for the final step in the process. Any remaining surface damage was removed by electropolishing approximately 100 μm from the gage diameter with a 10% perchloric, 90% methanol solution. The specimens were fatigued in the tension-compression mode on a Tatnell-Krause fatigue machine with constant stress amplitude and zero mean stress. The applied stress amplitude corresponded to one-half of the static yield stress, and the number of cycles (10^4) to which the alloy was subjected corresponded to about one-tenth of the expected fatigue life.

The X-ray double crystal diffractometer method combined with X-ray reflection topography (Berg-Barrett Method, hereafter referred to as B-B Method) was employed as the principal research tool of structural analysis. The X-ray rocking curves were taken in the n_x, $-n_y$) arrangement where n refers to the order of reflection and x and y to the first crystal and test crystal, respectively. In this type of arrangement the normals to the crystal surfaces are opposite in direction. A dislocation-free silicon crystal in the (111) orientation was used as the first, monochromating crystal, and the Cu $K\alpha_2$ reflection was eliminated with a knife edge. B-B topographs taken at angular rotation positions of the rocking curves allowed for correlation between the configuration of the defect structure and detailed features of the rocking curves.[20-28] The lattice defects induced by fatigue cycling of the Al 2024 alloy were studied by a double crystal diffractometer method developed for application to polycrystalline materials. This method related the analysis of the rocking curves of the reflecting grains to their topography and morphology.[21,23-26] In applying this method each reflecting grain of the specimen is considered to function independently as the second crystal of a double crystal diffractometer. With a reflected beam from the (111) face of a silicon crystal as the incident beam on the specimen, and carrying out angular specimen settings and appropriate film shifts between the settings produces pictorial rocking curves for each reflecting grain. The rocking curve is manifested as an array of spots of rising and falling intensity as the grain is rotated through its angular range of reflection, as shown by figures 9, 10, and 11 (see pages 15-17. Berg-Barrett topographs taken at the specimen surface correlate the topography and morphology of the grains to the corresponding rocking curves.

MAGNETIC PERMEABILITY

The induced voltage measurements were performed as depicted in figure 2.

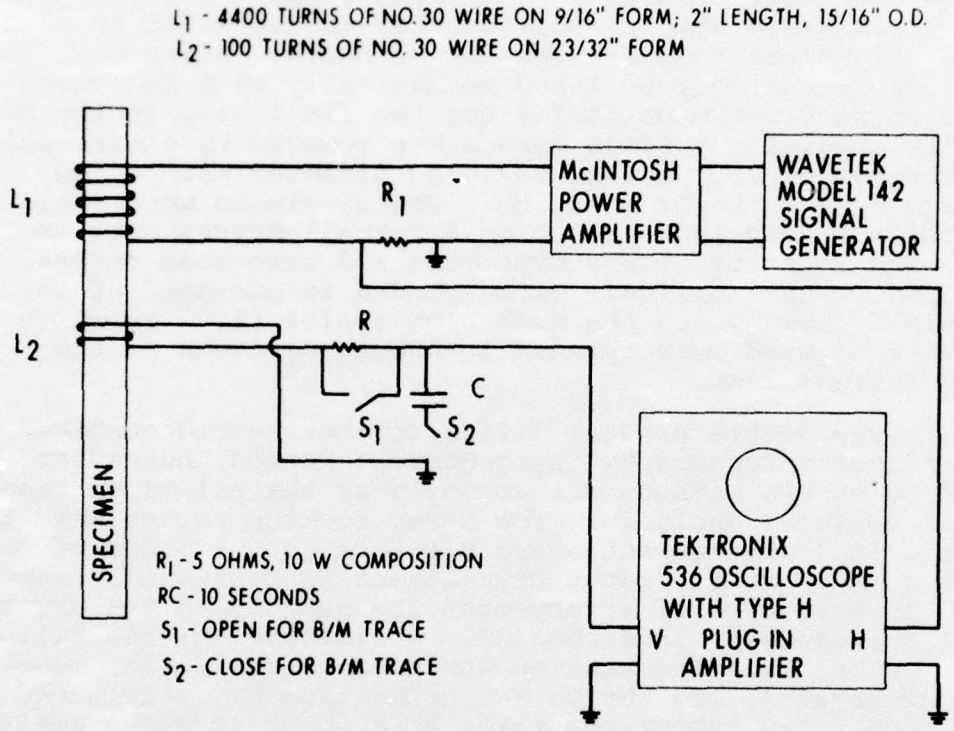

Figure 2
Arrangement for Induced Voltage Measurement
and B/H Curve Trace

The alternating magnetic field is produced by driving L_1 at the desired level and frequency. Current levels in L_1 are estab lished by monitoring the potential drop across the current-sensing resistor R_1 which also provides the horizontal axis of the display. The voltage induced in the secondary coil L_2 is impressed across the vertical axis. Vertical axis gain is adjusted so that both horizontal and vertical peak deflections are identical. By measuring the amplifier gains at which this occurs, the relative amplitude of the voltage induced in L_2 may be determined. The resultant elliptical Lissajou figure seen on the oscilloscope display is easily converted to phase angle as shown in detail in appendix C. A Polaroid photograph of the elliptical trace with a superimposed calibration signal preserves the data for future analysis. A minor modification of this arrangement was used to display the B/H hysteresis curve. This was accomplished by integrating the electromotive force induced on the secondary L_2 by means of the simple RC integrating circuit

shown in figure 2. The mathematical treatment for the B/H trace is straightforward and is given in appendix D. The specimen was demagnetized prior to all measurements by bringing it up to saturation at low frequency (5 Hz) and then gradually decreasing the amplitude of the magnetic field until it vanished. As may be seen from our previous discussion, this assured measurement of the initial permeability, μ_o. Coil impedance measurements utilized the bridge circuit shown in figure 3.

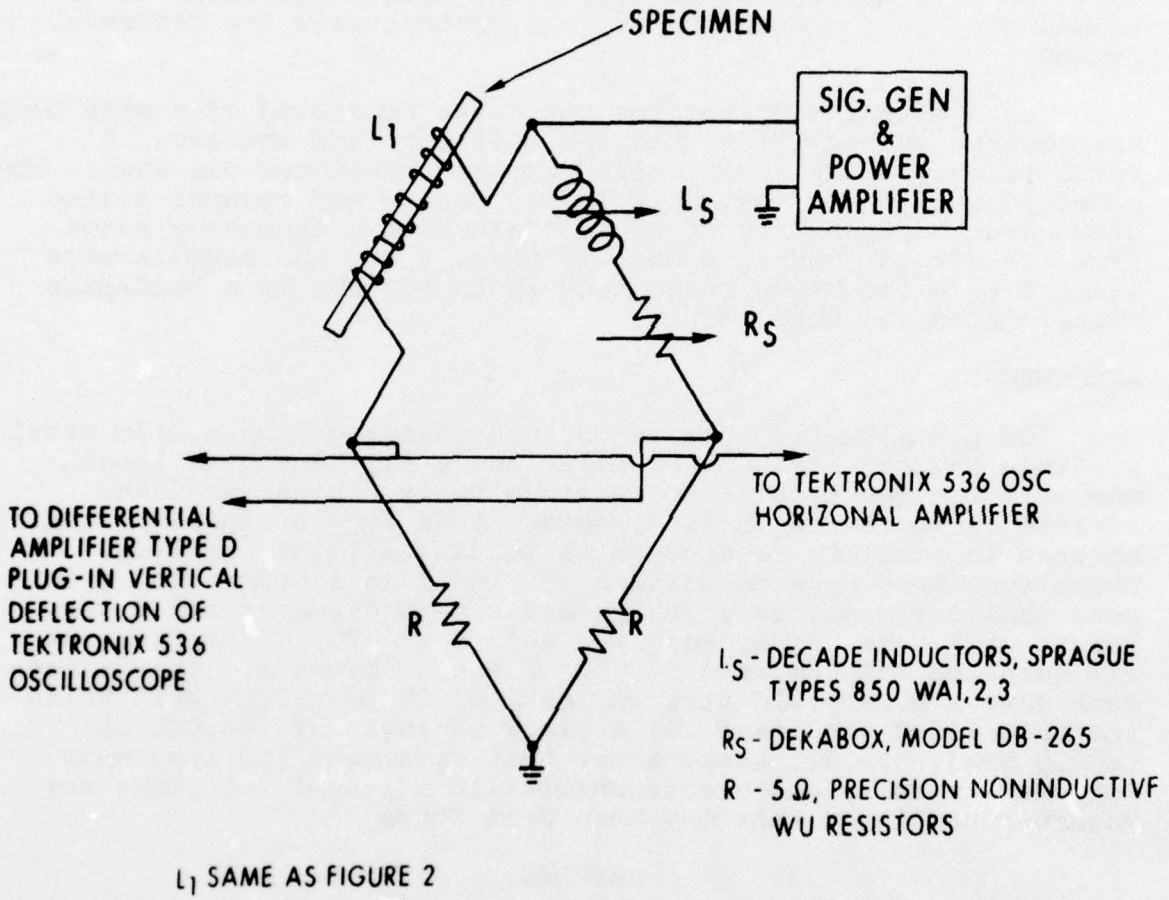

Figure 3
Low Frequency Impedance Measurement Arrangement

The coil surrounding the specimen was the same as L_1 in figure 2. Current levels through the coil were maintained in the linear region of the B/H characteristic. The standard inductance L_S and resistor R_S are adjusted until the output of the differential amplifier as displayed on the oscilloscope indicated a null. Readings of the L_S and R_S settings were subsequently corrected for the inevitable small resistive component in L_S and inductive component in R_S.

ACOUSTIC EMISSION

The acoustic emission measurements were made at the Johns Hopkins University in tensile machinery designed for quiet operation. The load was applied in a continuous manner by running water from a storage tank located above the testing machinery into a container at the end of the lever arm (15:1 mechanical advantage). A uniform flow rate was obtained by maintaining a constant pressure head in the storage tank. It should be noted that the grip configuration allows the direct placement of the transducers on the specimen without contact with the deforming region.

The monitoring system for the tests consisted of a wide band transducer, preamplifier, band-pass filter, and counter. A Parametrics 500 kHz (critically damped) transducer was used. The combined amplifier (Tektronix 1A7A), preamp and counter system used has the capability of 280-dB gain over a frequency range from 100 kHz to 3 MHz, ±3 db. In these tests the signals were limited to a frequency range from 75 to 200 KHz by a band-pass filter (Kronhite model 3202).

SPECIMENS

For the magnetic portion of this investigation a 4130 steel specimen having a 12.5-mm diameter and a 177.8-mm gage length was used for the tensile and fatigue tests. Because of the adverse ratio of length to diameter, this type of specimen cannot be used in complete reverse axial loading without buckling. These specimens were normalized at 815° C in 1 hour. The specimens used for acoustic emission had a 4-mm diameter and a gage length of 7.6 mm. They were austenized at 870° C for 25 minutes, oil quenched and tempered at 560° C for 30 minutes. This treatment gave a 0.2% yield strength of 156,000 psi (1076 MPa) while the normalized specimens had a yield strength of 100,000 psi (689.5 MPa). In all cases after heat treatment the specimens were mechanically and electrochemically polished to remove any decarburized layer that may have been formed.

RESULTS

X-RAY ROCKING CURVES

A typical halfwidth value of the rocking curve of an undeformed silicon crystal was about 15 seconds of arc. After 10% tensile deformation at 650° C the rocking-curve profile becomes multipeaked as shown in figure 4(a), and the extent of the halfwidth β pertaining to the principal peak was 935 seconds of arc. Surface layers were removed by chemical polishing in steps of 30, 100, 175, and 250 μm. Figure 4(b) shows the rocking-curve profile after removal of surface layers totaling 250 μm. Both the total range of reflection and the halfwidth of the subpeaks decreased drastically.

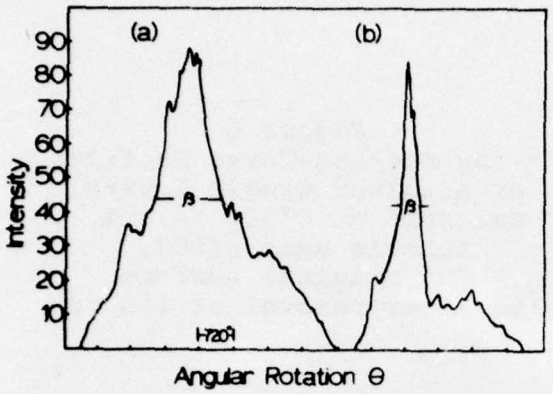

Figure 4 - X-ray Rocking-Curve Profiles of Silicon Single Crystal Deformed at 605° C, ϵ = 10%, tensile axis [110]. (a) Original surface (b) After removal of 250 μm

The dislocation gradient from surface to bulk was calculated from the relation given by Hirsch:[7] $D = \beta^2/9b^2$, where D is the number of excess dislocations of one sign, β is the measured halfwidth, and b is the magnitude of the burger vector. The variation of dislocation density with distance from the surface is shown in figure 5. It may be seen that after removal of about 100 μm the dislocation density was virtually that of the bulk material.

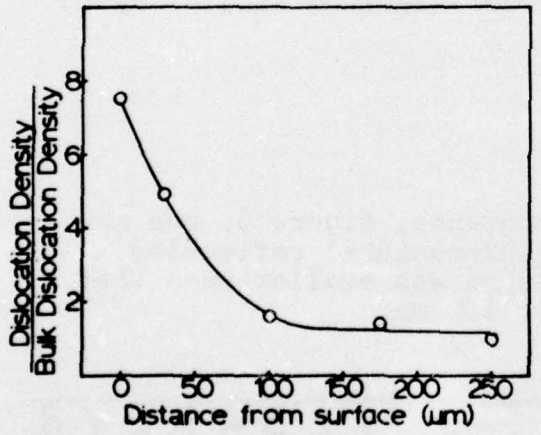

Figure 5
Dislocation Density Gradient from Surface to Bulk for Silicon Single Crystal

Tensile deformation of aluminum to 10% strain at 0° C also resulted in a multipeaked rocking curve as shown in figure 6(a). The lattice misalignment expressed in terms of the β value increased fourfold compared to the annealed crystal. Figure 6(b) shows the rocking-curve profile after surface removal of 100 μm. It may be observed that the total lattice misalignment as well as the halfwidth values decreased. The dependence of the ratio of dislocation density of surface layers to bulk density as a function of depth distance is shown in figure 7.

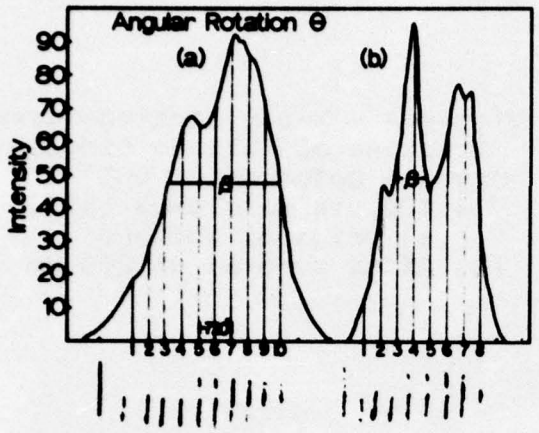

Figure 6
X-ray Rocking-Curve Profiles of Aluminum Single Crystal Deformed at 0° C, ε= 10%, tensile axis [100].
(a) Original surface
(b) After removal of 100 μm

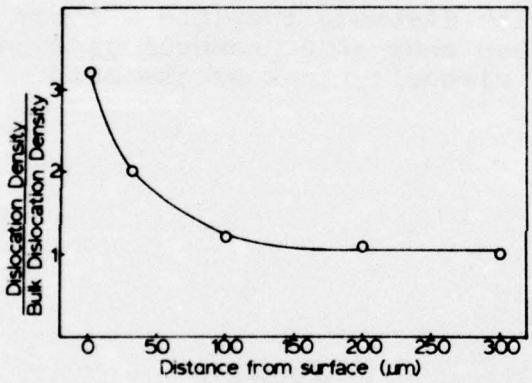

Figure 7
Dislocation Density Gradient from Surface to Bulk for Aluminum Single Crystal

Focusing attention on the B-B topographs, figure 8, one may note that the average size of the substructural reflecting domains pertaining to the surface layer was smaller than that obtained after removal of a layer of 100 μm.

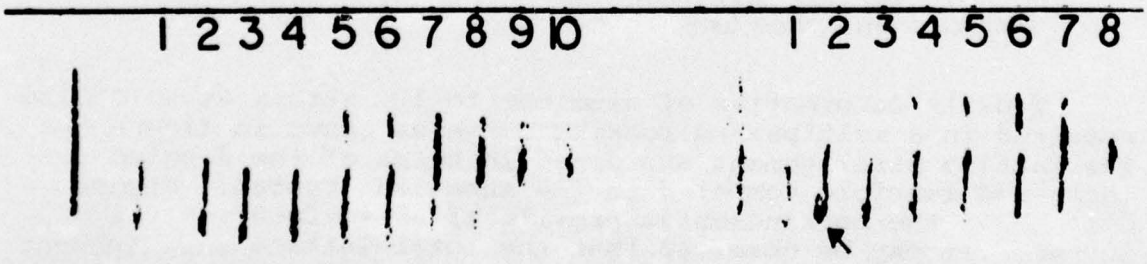

Figure 8 - X-ray Reflection Topographs Correlated to Rocking-Curve Profiles in Figure 6. First image corresponds to rotation over entire reflecting range; topographs numbered 1-10 and 1-8 correspond to angular positions indicated on profiles 6(a) and 6(b), respectively.

Moreover, the individual substructural domains in the surface layer remained in reflecting position over a much larger angular range than those in depth. For example, the large reflecting domain marked by an arrow went out of reflection after an angular rotation of only 360 seconds.

The structural investigation of the fatigued polycrystalline 2024 alloy was carried out by using a special X-ray double crystal diffractometer technique development for polycrystalline materials.[81,83-86] Item (a) of figure 9 shows the arrays of spots corresponding to the different grain reflections of the alloy prior to fatigue cycling.

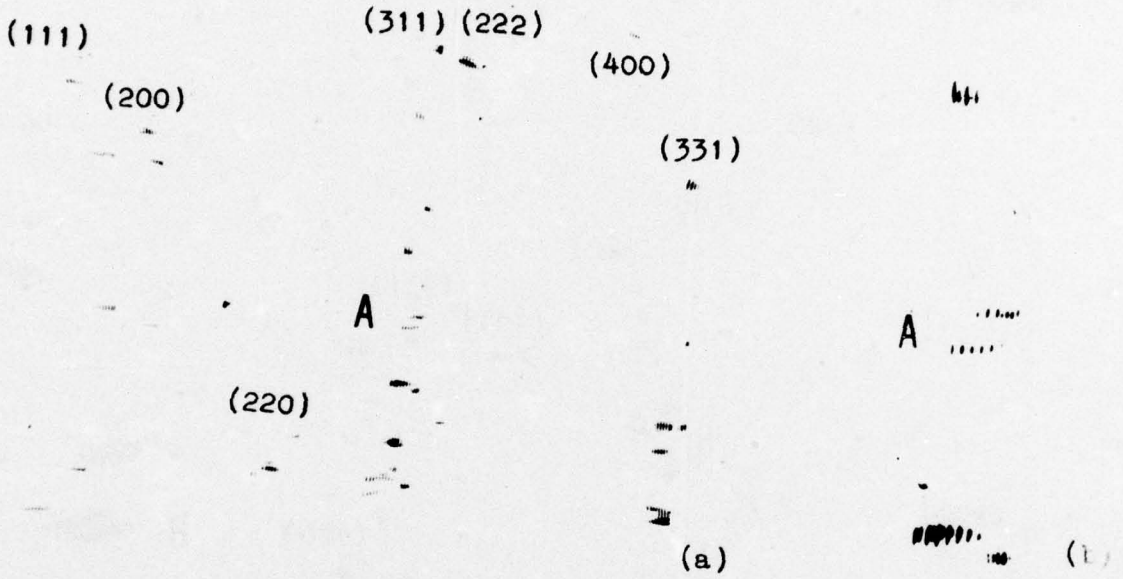

Figure 9 - Rocking Curves of Grain Reflections of 2024 Al prior to Cycling. Cu K monochromated radiation. Angular specimen settings 5' of arc.
(a) Overall survey of grain reflections
(b) Detail of range of reflection of grain A.

The discrete angular rotation of the specimen between consecutive spot reflections was 5 minutes of arc. Because a crystal monochromated beam impinged on the specimen having an average grain size of about 100 μm, relatively few grains were in reflecting position. Consequently, the spot reflections along the Debye-Scherrer ring appeared distinct and well separated. The rocking curves at high azimuthal angles, that is, at locations far removed from the equatorial reflections, became artificially broadened due to the contribution of the vertical divergence of the incident beam,[84] which is unaltered by reflection from the first crystal. It is most convenient, therefore, to focus

attention on the equatorial reflections, such as spot reflection A in figure 9, since for these the contribution of the vertical divergence to broadening is zero. It can be seen that for grain A the angular range of reflection was traversed after five spot settings, thus amounting to about 25 minutes of arc (item (b) of figure 9). Arrays of spots pertaining to other grain reflections exhibited similar or even smaller values. By contrast, the grain reflections in item (a) of figure 10 pertaining to the cycled specimen not only exhibited a much larger angular range, manifested by the extended arrays of spot reflections, but also showed the typical image distortions characteristic of a substructure induced by deformation. These two aspects can be seen from the equatorial grain reflection B (item (b) of figure 10) which, like the grain reflection A, pertains to the (311) reflection.

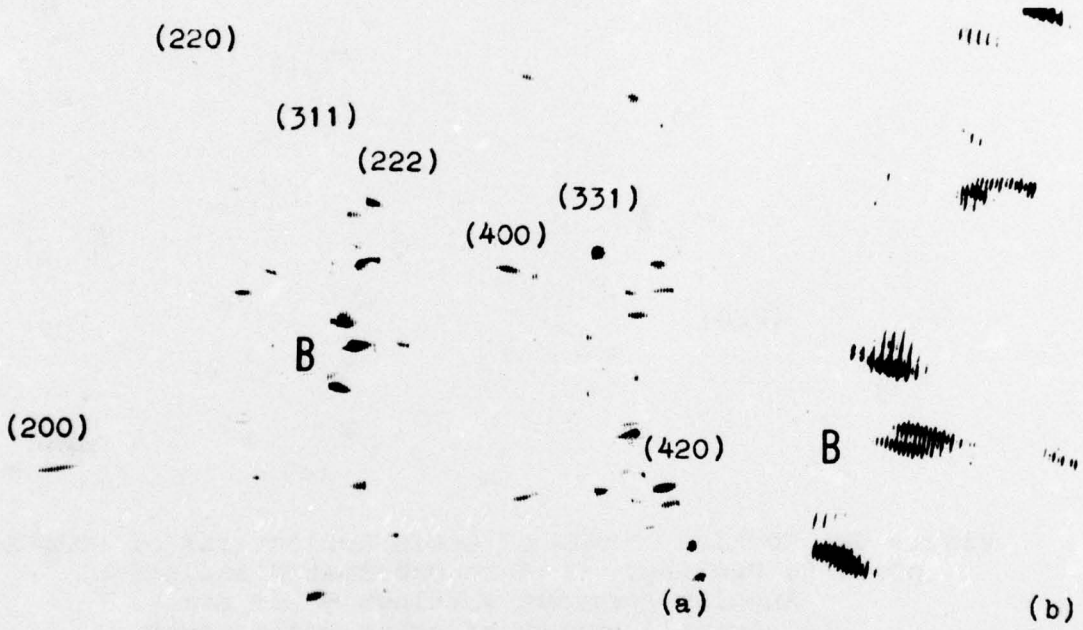

Figure 10 - Rocking Curves of Grain Reflections of Cycled 2024 Al (N = 10^4).
Cu K monochromated radiation.
Angular specimen setting 5' of arc.
(a) Overall survey of grain reflections.
(b) Detail of range of reflection of grain B.

Grain B exhibited two multipeaked arrays displaced with respect to each other. The total halfwidth of the rocking curves covered about 18 spot settings or 18 x 5 minutes or ~ 1.5 degrees of arc. The multipeaked intensity distribution was due to the substructural lattice comains which were sequentially brought into

and out of reflecting position as the grains were rotated through the angular range of reflection. The multipeaked nature of the intensity curve was quite analogous to that obtained for large tensile-deformed aluminum single crystals shown in figure 6. After removal of a surface layer of 100 μm from the cycled specimen the image distortions of the spot reflections decreased and the average halfwidth value of the rocking curves β was diminished as may be seen from figure 11 (viz, grain reflection C).

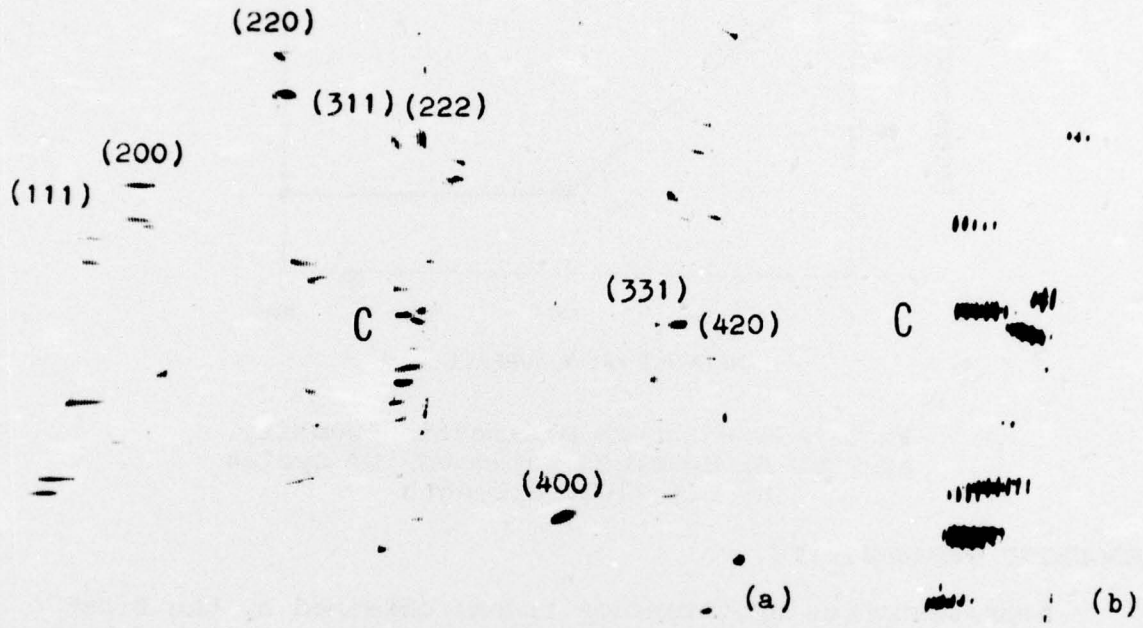

Figure 11 - Rocking Curves of Grain Reflections of Cycled 2024 Al after Removal of 100 μm Surface Layer.
Cu K monochromated radiation.
Angular specimen settings 5' of arc.
(a) Overall survey of grain reflections.
(b) Detail of range of reflection of grain C.

Typical values were between 40 and 50 minutes of arc. Using the average β values for the cycled specimen of 90 minutes at the surface and 45 minutes at a depth of 100 μm, one obtains a decrease in the density of excess dislocations from 23.1×10^9 to 5.8×10^9 (i.e., a reduction by a factor of about 4). An examination of the specimen after removal of 200 μm gave an excess dislocation density of the same value as that at 100 μm. The excess dislocation density as a function of depth is given in figure 12.

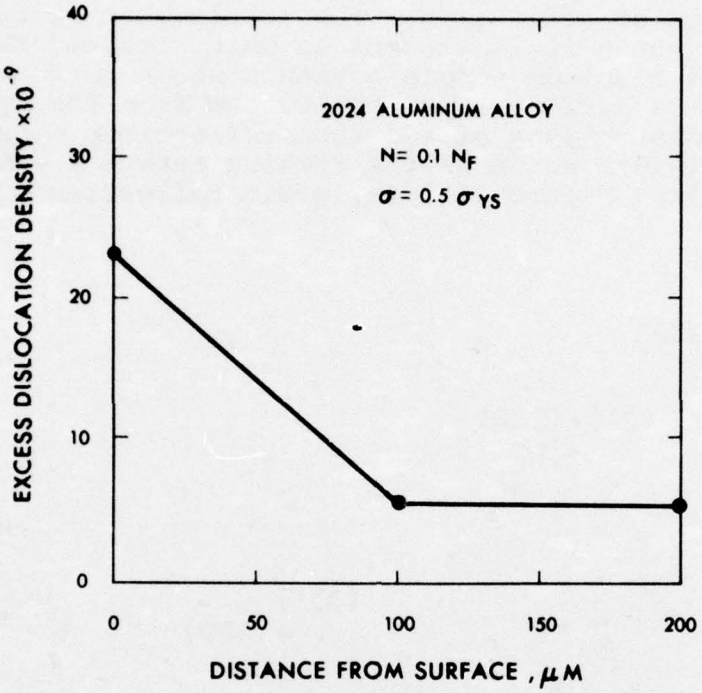

Figure 12 - Excess Dislocation Density of 2024 Al Specimen Fatigued 10^4 Cycles at 0.5 Yield Strength

MAGNETIC PERMEABILITY

Representative oscilloscope traces obtained by the first method described above for a 4130 steel specimen that had been strained 0.4% is shown in figure 13. The amplitudes A and the phases of the induced voltage Φ are given in table 2. These data show that after straining 0.4% the amplitude of the induced voltage A decreased. However, the phase angle Φ between the input and output voltage remained relatively unchanged. These measurements were found to be sensitive to the relative disposition of L_1 and L_2 (see figure 2). Although care was taken to assure that the contribution of this extraneous factor was minimal, it was decided to verify the findings up to this point and to attain a potentially more discriminating technique for observing phase-angle changes. Consequently, a specimen, strained plastically approximately 2%, was measured both prior to and subsequent to deformation by using the impedance measuring arrangement shown in figure 3. The resultant uncorrected data are shown in table 3. Tedious but straightforward corrections for the resistance of the inductors at the various frequencies as well as the stray inductance of the standard resistors must be made. The basic data for these corrections are summarized in table 4. It is evident that, confirming the earlier findings for the specimen strained 0.4%, the deformation resulted in a marked decrease

in measured inductance at very low frequencies coupled with a decrease in the measured resistance at the higher frequencies.

(a) - Initial Trace

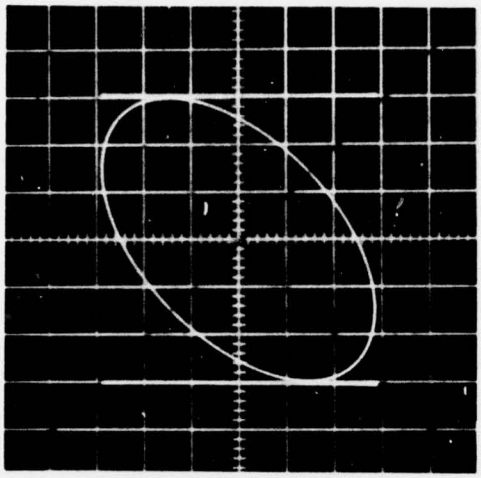

(b) - After Deformation

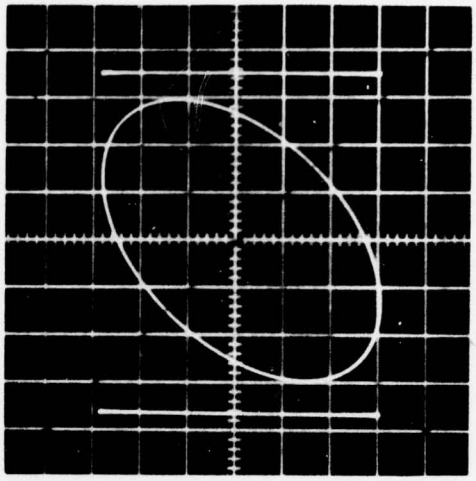

(c) - Initial Trace

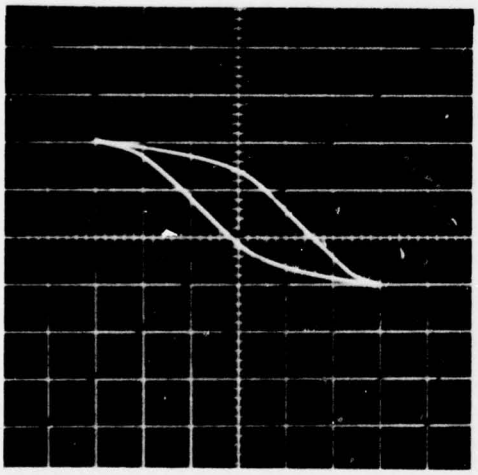

(d) - After Deformation

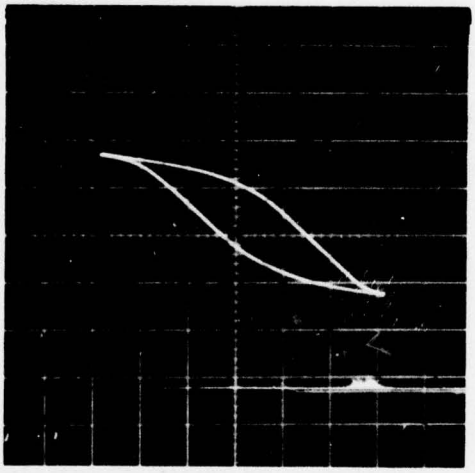

Figure 13 - (a) (b) - Trace of Voltage across L_2 versus Current through L_1;
(c) (d) - Trace of Integral of Voltage across L_2 versus Current through L_1

TABLE 2 - AMPLITUDE AND PHASE OF INDUCED VOLTAGE FOR UNSTRESSED AND STRESSED SPECIMENS OF 4130 STEEL STRAINED 0.4%

Frequency Hz	A(1)* mv	A(2)* mv	∅(1)**	∅(2)**
5	6	4.5	0.81	0.83
10	11	9.4	0.82	0.84
20	21	18.5	0.75	0.79
50	50	41.5	0.60	0.60
100	76	65	0.405	0.44
200	100	85	0.32	0.32
500	137	111	0.229	0.214
1000	162	127	0.167	0.157
2000	182	140	0.16	0.128
5000	200	158	0.112	0.112
10,000	231	182	0.112	0.143

*Peak-to-peak amplitude of induced voltage for a primary current of 25 mA peak to peak; A(1) unstressed, A(2) stressed.

**Ratio of minor to major axis of ellipse; convert to phase angle; from theory in appendix C; ∅(1) unstressed, ∅(2) stressed.

TABLE 3 - IMPEDANCE MEASUREMENTS OF 4130 STEEL UNSTRAINED AND STRAINED 2%

	L, henries		R, ohms*	
Frequency, hz	Unstrained	Strained 2%	Unstrained	Strained 2%
5	1.065	0.869	86	100
10	1.015	0.868	92	102
20	1.017	0.861	102	110
50	0.922	0.809	165	154
100	0.771	0.698	285	258
200	0.624	0.558	455	419
500	0.468	0.412	840	753
1,000	0.377	0.329	1,350	1,190
2,000	0.306	0.266	2,080	1,828
5,000	0.227	0.200	4,000	3,400
10,000	0.186	0.166	6,900	5,800

*Readings must be corrected for resistance of standard inductors, also one must subtract fixed resistor of 105 ohms in series with L_1 inserted to allow balance at lower frequencies.

TABLE 4 - CORRECTION FACTORS FOR SPECIMEN

Resistance of Standard Inductors

L Setting, henries x 10^{-3}	R ohms	L Setting, henries x 10^{-2}	R ohms	L Setting, henries x 10^{-1}	R ohms
1	0.26	1	0.92	1	8.55
2	0.35	2	1.54	2	15.1
3	0.54	3	2.38	3	23.6
4	0.48	4	2.80	4	28.4
5	0.68	5	3.67	5	36.9
6	0.78	6	4.30	6	43.5
7	0.96	7	5.15	7	52.0
8	1.02	8	5.97	8	61.6
9	1.09	9	6.57	9	68.2
10	1.26	10	7.42	10	76.6

Inductance of Standard Resistors (at 10 kHz)

R Setting ohms	Inductance mH	R Setting ohms	Inductance mH
100	0.3	900	2.9
200	0.7	1,000	3.3
300	1.0	2,000	6.5
400	1.3	3,000	9.5
500	1.6	4,000	13.0
600	1.9	5,000	16.0
700	2.2	6,000	19.0
800	2.5	7,000	22.0

To determine the effect on the impedance of the reduction in diameter of the specimen strained 2%, an unstrained specimen was electropolished to reduce the diameter the same amount (0.25 mm). Impedance measurements were made before and after the metal removal. From these data it was apparent that the reduction in the diameter did not account for the major changes observed in the strained (2%) specimens.

ACOUSTIC EMISSION

The acoustic emission behavior was investigated on specimens of 4130 steel that had been fatigued at 90 and 125 ksi after 1 cycle and after 25%, 50%, and 75% of the fatigue life. It was quite apparent in all cases that emissions occurred at stresses quite far below those at which the specimens had been fatigued. This portion of the investigation was not conducted in sufficient depth to determine the reasons for the nonexistance of the Kaiser effect; however, from the acoustic emission

research currently under way by Carpenter,[28] it appears that the magnetostriction properties of steels are important. Such properties cause the domain configuration to be determined in part by the internal stress fields. Applying a load will cause rapid changes in the domain configuration in the manner of the Barkhausen effect.[13] These changes will be the source of elastic waves via the changes in the magnetic structure that will be sensed by the pickup transducer. Still another possibility for the low stress emissions is relaxation. However, it appears that the emissions occur at too low a stress relative to the prestress to be accounted for by such as mechanism.

DISCUSSION

The X-ray line broadening and topography study shows that tensile deformation in such diverse materials as silicon and aluminum resulted in a preferential deformation of surface layers compared to that of the bulk material. In aluminum, the deformed surface layer exhibited not only smaller misaligned lattice domains than those in depth but also the larger angular range over which the individual substructural reflections persisted was indicative of a greater density of excess dislocations within these domains. The substructural features of the surface layer may be likened to a lattice "debris," whereas those in depth are more like the substructure of the annealed material. The differentiation is attributed to preferred activation of dislocation sources located near the surface[29] and to intense interaction of moving dislocations on multiple slip systems. Kitajima[30-31] came to similar conclusions using etch-pit techniques for the characterization of the dislocation structure in deformed copper. Kramer[29,32-34] has reported previously that work hardening does not occur uniformly throughout a uniaxially strained specimen and is greater in the surface layer than in the interior. He reporte that this surface layer also forms in stage I of fcc metals where only single slip is supposed to operate.

The preliminary results obtained from the fatigue cycled Al 2024 alloy indicate a strong adherence to the "debris" concept.[35] The X-ray images derived from the reflecting grains of the undeformed material were uniform and passed quickly in and out of reflection, viz, 20 to 25 minutes of arc. In contrast, when a specimen was subjected to 10,000 fatigue cycles at a stress amplitude amounting to 0.5 of the yield stress of the material, the images persisted over a large angular range, viz, 90 minutes of arc, and were broken up indicating the formation of a highly misoriented surface layer. In addition, the intensity of the spots increased significantly over their undeformed counter parts signifying an increase in integrated intensity with the broadening of the associated rocking curves. The reflections emanating from greater depths of the material and identified by their weakness relative to surface reflections of the same crystallographic order were found to be highly regular and short in reflecting range. This suggests that the bulk material did not incur as much damage as the surface layer as a result

of fatigue cycling. The X-ray results obtained after a surface layer of 100 μm had been removed confirmed the greater degree of crystal perfection since the reflection curves became narrower, vis, 45 minutes of arc, and the break-up of the grain reflections into substructural units declined. Electron microscope studies by Duquette and Swann provided similar evidence of high surface layer dislocation densities in a low-strain, fatigue-cycled aluminum alloy.[38]

With reference to the cause of the magnetic measurement changes upon deformation of specimens strained 0.4% and 2%, the data in table 3 show that there is a pronounced decrease in the measured inductance at the low frequency of 5 Hz after deformation. From equation (14a) and figure 1 it may be seen that $\mu_{eff.r} \approx 1$ for very low frequencies (small f/f_g); consequently, a decrease in inductance must be attributed to a decrease in μ. A more quantitative estimate of f/f_g for the specimens in question is contained in appendix E. These estimates confirm that f/f_g is very small for $f = 5$ Hz. Some supplemental measurements of specimen resistance were made by using a Kelvin bridge. The resistance was found to be approximately 4.3 milliohms for all specimens and was relatively unchanged by plastic deformation, thereby confirming the conclusion that measurement changes were due to changes in the initial permeability μ_o. The changes in permeability close to the surface may be estimated with the aid of equation (14b) applied to the highest frequency measurements, equation (14a) being insensitive to higher frequencies results due to the dominance of the $1 - \eta$ term. From this equation it is easily seen that

$$\Delta R'/R' = \Delta\mu/\mu + \Delta\mu_{eff.i}/\mu_{eff.i} \qquad (15)$$

where $R' = R - R$. From equation (13) and table 1, $\Delta\mu_{eff.i}/\mu_{eff.i}$ may be related to $\Delta\mu/\mu$. At the very highest frequencies $\Delta\mu_{eff.i}$ is independent of μ. At lower frequencies the relationship may be approximated as is shown in appendix F. The main point is that a decrease in μ at these frequencies is partially compensated by an increase in $\mu_{eff.i}$ so that the overall change in R' is diminished. By applying this to the data the change in μ may be estimated and compared to the change in μ at 5 Hz (equation (14a) as developed in appendix G). The results of these calculations are summarized in table 5. From these it is seen that the plastically deformed specimens seen to exhibit substantially larger changes in μ at higher frequencies.

TABLE 5
CHANGE IN μ at
LOW AND HIGH FREQUENCIES

Strain %	Frequency	$\Delta\mu/\mu$
0.4	5 Hz	-0.27
	10 kHz	-0.42
2	5 Hz	-0.20
	10 kHz	-0.35

Some mention should be made of the effective depth of permeability measurement. Calculations of skin depth as a function of f/f_g for specimens of cylindrical geometry have appeared in the literature.[16] Applying the results to the specimens reported herein yields the skin depths listed in table 1-F of appendix F. It is seen that the skin depth for the highest frequency 70kHz is approximately 125 μm, which depth would appear to be the desired order. However, it should be realized that depth varies inversely as $\mu^{1/2}$. Consequently, a decreasing μ will result in a greater skin depth and the consequent change in measured parameters counter to that produced by the decrease in μ. This makes the overall technique somewhat less sensitive than it would appear to be at first sight. However, the limited data obtained thus far would indicate that radial variations of μ are obser vable.

Not much mention has been made of coercivity measurements, although the oscilloscope displays shown in figure 13 would allow its estimation throughout the entire cross section. At higher frequencies, eddy currents confounded the display to a point where simple interpretation was not possible. Furthermore, the effects of the demagnetizing field at the ends of the specimen are not easily ascertained, although it may be shown shown[12,37] that the effects on measured permeability were negligible for the specimen geometries and ranges of permeability under consideration. Consequently, this particular measurement technique offered little in the way of measurement of the coercivity in the surface layer and so was not pursued further.

CONCLUSIONS

- From the X-ray line broadening and B-B topographic measurement it was quite evident that the excess dislocation density in the surface layer was much greater than that in the bulk for specimens that had been fatigued or strained unidirectionally.

- From the measurements on plastically deformed steels that showed that the initial permeability decreased at

high frequencies (10 kHz), it could also be inferred that the dislocation density was larger in the surface layer than in the bulk.

- Because emissions occurred at relatively low stresses after fatiguing at high stress amplitudes, it appears that acoustic emission cannot be used to detect fatigue change in ferromagnetic materials. While such a technique may possibly be used in the laboratory, it could not be used in the field unless the magnetic domains can be prevented from growing. There is a possibility that acoustic emission may be useful for nonmagnetic materials - provided other emission sources do not operate.

FUTURE WORK

During the following year emphasis will be placed on the X-ray rocking curve of polycrystalline aluminum and magnetic permeability of steel. The line widths will be measured as a function of the fraction of fatigue life. For the magnetic permeability portion of this effort measurement at higher frequency (>10 kHz) will be investigated to obtain improved sensitivity.

TECHNICAL REFERENCES

1 - Kramer, I.R., Proc. Air Force Conference on Fatigue and Fractures, AFFDL-TR-70-144 (1969)
2 - Kramer, I.R., Met. Trans., Vol. 5, p. 1735 (1974)
3 - Seeger, A., Dislocations and Mechanical Properties of Crystals, New York, John Wiley & Sons, Inc., p. 243 (1956)
4 - Taira, Shuiji, et al, Proc. 13th Japanese Congress on Materials Research, p. 14 (1970)
5 - Thomas, D.J.D., Phys. Status Solidi, Vol. 3, p. 2261 (1963)
6 - Fisher, A.W., and J.A. Amick, J. Electrochem. Soc., Vol. 113, p. 1054 (1966)
7 - Lawrence, J.E., J. Appl. Phys. Vol. 40, p. 360 (1969)
8 - Ravi, K.V., J. Appl. Phys. Vol. 43, p. 1785 (1972)
9 - Alexander, H., Z. Metallkde, Vol. 52, p. 344 (1961)
10 - Brown, W.F., Jr., Physical Review, Vol. 60, p. 139 (July 1941)
11 - Kersten, M., Z. Tech. Phys., Vol. 12, p. 665 (1931)
12 - Bozorth, R.M., Ferromagnetism, Princeton, D. Van Nostrand Co., Inc. (1951)
13 - Gardner, G.G., et al, International Journal of Nondestructive Testing, Vol. 3, p. 131 (1971)
14 - Saynojakaugas, S., and M. Otala, IEEE Transactions on Magnetics, Vol. 9, No. 4, p. 641 (1973)
15 - Abaku, S., and B.D. Cullity, Experimental Mechanics, p. 217 (1971)
16 - McMaster, R.C., ed., Nondestructive Testing Handbook, Vol. II, R.C. McMaster, ed. New York, The Ronald Press Co. (1963)

17 - Foerster, F., Z. Metallkde, Vol. 45, p. 182 (1954)
18 - Kaiser, J., Untersuchungen uber das Auftreaten von Gerauschen beim Zugversuch," Ph.D. Thesis, Tech. Hochsch, Muchen (1950)
19 - Duke, J.C., and R.A. Kline, Acta. Met., Vol. 9, p. 855 (1975)
20 - Intrater, J., and S. Weissmann, Acta Cryst., Vol. 7, p. 729 (1954)
21 - Weissmann, S., J. Appl. Phys., Vol. 27, p. 389 (1956)
22 - Weissmann, S., et al, "Recovery and Recrystalization of Metals," Interscience, pp. 241-267 (1963
23 - Reis, J.J., et al, J. Appl. Phys., Vol. 22, p. 665 (1951)
24 - Slade, J.J., Jr., and S. Weissmann, J. Appl. Phys., Vol. 23, p. 323 (1952)
25 - Weissmann, S., and D.L. Evans, Acta. Cryst., Vol. 7, p. 733 (1954)
26 - Weissmann, S., J. Appl. Phys., Vol. 27, p. 1335 (1956)
27 - Hirsch, P.B., "Mosaic Structure," Prog. Met. Phys., Vol. 6, p. 283 (1956)
28 - Carpenter, S.H., and F.H. Higgins, University of Denver, private communication (1976)
29 - Kramer, I.R., Trans. Am. Inst. Min. Engs., Vol. 227, p. 1003 (1963)
30 - Kitajima, S., "Study of Yielding and Easy Glide Deformation of Highly Perfect Copper Crystals by Using Etch-Pit Techniques," NATO Advanced Study Institute, Surface Effects in Crystal Plasticity, Hohegeiss, West Germany (Sep 1975)
31 - Kitajama, S., et al, Trans. J. I.M., Vol. 10 (1969)
32 - Kramer, I.R., Trans. Am. Inst. Min. Engs., Vol. 230, p. 991 (1964)
33 - Kramer, I.R., Trans. Am. Inst. Min. Engs., Vol. 233, p. 1462 (1965)
34 - Kramer, I.R., and N. Balasubramanian, Acta. Met., Vol. 21, p. 695 (1973)
35 - Kramer, I.R., Trans. ASM, Vol. 62, p. 521 (1969)
36 - Duquette, D.J., and P.R. Swann, Acta Met., Vol. 24, p. 241 (1976)
37 - McClury, G.O., Nondestructive Testing, Vol. 13, No. 1, p. 23 (1955)

APPENDIX A

RELATIONSHIP OF INTERNAL STRESS TO INITIAL PERMEABILITY

REFERENCES

(a) Kersten, M., Z. Tech. Physical, 12 Vol. 12, p. 665 (1931)
(b) Bozorth, R.M., Ferromagnetism, Princeton, D. Van Nostrand Co., Inc., (1951)

This parallels the simplified derivation given in the early literature (reference (a)). First consider a magentic domain over which there is a uniform internal stress τ_i. In the absence of an applied field, the domain magnetization will assume a minimum energy direction, which direction is parallel to τ_i for materials with positive magnetostriction. If a magnetic field H is applied an an angle θ_o with respect to τ_i, then the magnetization of the domain I_s will rotate partially into this direction to some equilibrium angle θ (see figure 1-A).

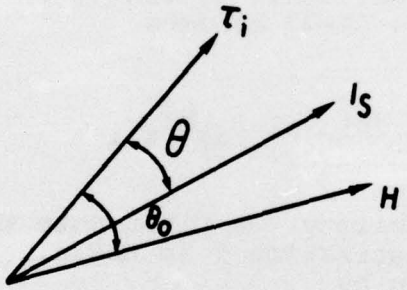

Figure 1-A
Vector Relationship
Among H, I_s, and τ_i

The angle θ is that which results in the total domain energy being a minimum. It can be shown (reference (b)) that the total ebergt E has two components, the strain energy $E_{\tau i}$ and the energy of a dipole in a magnetic field E_H, and that these are given by

$$E_{\tau i} = 3/2 \left(\lambda_s \tau_i \sin^2\theta\right) \qquad \text{(A-1)}$$

and

$$E_H = -HI_s \cos\left(\theta_o - \theta\right) \tag{A-2}$$

where λ_s is the magnetostrictive coefficient at saturation and I_s is the saturation magnetization per unit volume. The condition for equilibrium is that

$$dE/d\theta = 0; \text{ where } E = E_{\tau i} + E_H \tag{A-3}$$

Applying this condition results in

$$3\lambda_{s\ i} \sin\theta \cos\theta = HI_s \sin\left(\theta_o - \theta\right) \tag{A-4}$$

For small H and consequent small θ, $\sin\theta = \theta$, $\cos\theta \sim 1$ and $H\theta \sim 0$, so that equation (A-4) becomes

$$\theta = \left[HI_s \sin\theta_o\right]/3\lambda_s\tau_i \tag{A-5}$$

To calculate the permeability, we first note that for small applied fields the magnetization I in the direction of the applied field H is given by

$$I = kH \tag{A-6}$$

where k is the magnetic susceptibility. Since

$$B = H + I \tag{A-7}$$

by definition and since the permeability $\mu = B/H$ by definition as well, it is seen from equations (A-6) and (A-7) that

$$\mu - 1 = k = dI/dH = (dI/d\theta) \times (d\theta/dH) \tag{A-8}$$

Since the component of I_s in the direction of the field is given by

$$I = I_s \cos (\theta_o - \theta) \tag{A-9}$$

then

$$dI/d\theta = I_s \sin(\theta_o - \theta) \sim I_s \sin \theta_o \text{ for small } \theta \tag{A-10}$$

From equation (A-5) it is seen that

$$d\theta/dH = I_s \sin \theta_o / 3\lambda_s \tau_i \tag{A-11}$$

so that from equations (A-8), (A-10), and (A-11) we obtain

$$\mu - 1 = I_s^2 \sin^2 \theta_o / 3\lambda_s \tau_i \tag{A-12}$$

for an internal stress at an angle θ with respect to the applied field H. If we average this expression over all possible values of θ_o from 0° to 180° we obtain $\sin^2 \theta_o = 1/2$ over this interval, so that

$$\mu - 1 = I_s^2 / 6\lambda_s \tau_i \tag{A-13}$$

While this is only a very approximate expression, it tells us that permeability varies inversely with internal stress and that absence of stress should result in very large permeabilities. This does occur for highly oriented microstructures wherein the grains are oriented along the "easy" axis of magnetization. In a randomly oriented metal the magnetizing field must overcome the restoring forces of crystalline anisotropy as well so that, even in the absence of internal stress, the permeability would not be as high as predicted by equation (A-13). However, it shows that the presence of internal stress should decrease the permeability.

APPENDIX B
PENETRATION OF A VARYING MAGNETIC FIELD INTO A CONDUCTOR

REFERENCES

(a) Foerster, F., Z. Metallkde, Vol. 45, p. 182 (1954)
(b) Brown, W. F., Jr., Physical Review, Vol 60, p. 139 (July 1941)

This derivation is given primarily to expose the physical assumptions underlying most of the statements regarding the so called "skin effect" and thereby give the understanding required to appreciate the results of the investigations reported herein. We start with Maxwell's equations for a homogeneous, isotropic, linear medium

$$\nabla \times E = \frac{\partial B}{\partial t} \tag{B-1}$$

$$\nabla \times H = \frac{\partial D}{\partial t} + j \tag{B-2}$$

where E is the electric field intensity, H the magnetic field intensity, D the electric displacement, B the magnetic induction, j the current density, and t the time. Units need not be of concern at the moment. The major assumption made at this point is that for the electrical conductivities and frequencies of interest we may ignore the displacement current $\frac{\partial D}{\partial t}$ in comparison to the conduction current j; or

$$\nabla \times H = j \tag{B-3}$$

In addition, it is assumed that Ohm's law holds for the medium; i.e.,

$$j = \sigma E \tag{B-4}$$

where σ is the electrical conductivity, and further that

$$B = \mu H \tag{B-5}$$

where μ is the magnetic permeability. (This holds even for magnetized ferromagnetic materials provided H is sufficiently small, and the correct value is used for μ.) With these assumptions, equations (B-1) and (B-2) become

$$\nabla \times E = \frac{\mu \partial H}{\partial t} \tag{B-6}$$

$$\nabla \times H = \sigma E \tag{B-7}$$

Taking the curl of both sides of both equations and using the vector analysis identity

$$\nabla \times \nabla \times = \nabla\nabla \cdot - \nabla^2 \qquad \text{(B-8)}$$

and by manipulating to obtain isolated equations for E and H the following partial differential equation is obtained for H

$$\nabla^2 H = \mu\sigma \frac{\partial H}{\partial t} \qquad \text{(B-9)}$$

This is the vector equivalent of the heat conduction or diffusion equation which already has been solved for many practical cases of interest. With the aid of figure 1 of the text the simplest, planar solution may be derived. H is assumed to be parallel to the surface of a semi-infinite metallic region and to have the following simple time dependence external to the metal with no external spatial dependence;

$$H_z(x) = H_o \cos\ (2\pi ft);\ x \geq o \qquad \text{(B-10)}$$

Direct substitution in equation (B-9) for which we also assume $H_x \equiv H_y \equiv 0$ verifies that the following expression

$$H_z = H_o\ \epsilon^{x/s} \cos\ (2\pi ft - \frac{x}{s}) \qquad \text{(B-11)}$$

is a solution in the planar case satisfying the boundary condition (reference (17)), provided that

$$s = (\pi\mu\sigma f)^{-\frac{1}{2}} \qquad \text{(B-12)}$$

s is obviously the depth at which H decreases to 1/e times its value at the surface, x = 0.

In the cylindrical case, the boundary equation (B-10) remains the same for $r \geq r_o$, the radius of the cylinder. Equation (B-9) in cylindrical coordinates for $H_r = H = 0$ becomes

$$\frac{1}{r} \frac{\partial}{\partial r}\left(r \frac{\partial H_z}{\partial r}\right) = \mu\sigma \frac{\partial H_z}{\partial t} \qquad \text{(B-13)}$$

From the standard approach of separation of variables we assume

$$H_z = R(r)T(t) \qquad \text{(B-14)}$$

which yields

$$\frac{1}{rR} \frac{\partial}{\partial r}\left(r \frac{\partial R}{\partial r}\right) = \frac{\mu\sigma}{T} \frac{\partial T}{\partial t} = -\lambda^2 \text{ (constant)}$$

The equation in R is, upon appropriate transformation of variables, the zeroth order Bessel equation. Consequently, the solution for the spatial dependence of H turns out to be

$$H = H_o \left[\frac{ber^2 (2\theta r/d) + bei^2\left(\frac{2\theta r}{d}\right)}{ber^2 \theta + bei^2 (\theta)} \right] \qquad \text{(B-15)}$$

where the ber and bei functions are complex combinations of Bessel's functions and

$$\theta = d\sqrt{\frac{\pi \mu f \sigma}{2}} \qquad \text{(B-16)}$$

where d is the diameter of the cylindrical specimen.

Equation (B-15) provides the basis for computing the effective permeability μ_{eff} of a cylindrical specimen. The effective permeability is defined as that value that yields the total flux φ through the cross section of a cylindrical specimen in the following equation

$$\varphi = \pi r_c^2 \mu \mu_{eff} H_o; \; r_c = d/2 \qquad \text{(B-17)}$$

However, following the standard derivation (reference (a)), the total flux is obtained by summing the flux through each cylindrical shell of thickness dr as expressed by the equation below

$$\varphi = 2\pi\mu \int_o^{r_c} r H \, dr \qquad \text{(B-18)}$$

where H is given by equation (B-15). From equations (B-17) and (B-18) we have

$$\mu_{eff} = \frac{2}{H_o r_o} \int_o^{r_c} rHdr \qquad \text{(B-19)}$$

Upon integration, equation (B-19) yields (reference (b))

$$\mu_{eff} = \frac{2}{Kr_c} \frac{J_1(\alpha\theta/2)}{J_o(\alpha\theta/2)} \qquad \text{(B-20)}$$

where J_o and J_1 are Bessel functions of the zeroth and first order and α as a complex quantity is given by

$$\alpha = \sqrt{j}, \text{ where } j = \sqrt{-1} \qquad \text{(B-21)}$$

It follows that μ_{eff} is a complex quantity. In physical terms, this means that the flux through the specimen is out of phase with the applied magnetizing field.

APPENDIX C
COMPUTATION OF PHASE FROM AN ELLIPTICAL LISSAJOU FIGURE

Assume that the x and y axis deflections of an oscilloscope display are described by the following time parametric equations

$$x = r\sin(\omega t + \alpha_1) \tag{C-1}$$

$$y = r\sin(\omega t + \alpha_2) \tag{C-2}$$

That is, each axis deflection is sinusoidal, of equal amplitude, and of differing phase. Upon some manipulation and the use of a standard trigonometric identity, these become

$$x/r = \sin\omega t\cos\alpha_1 + \cos\omega t\sin\alpha_1 \tag{C-3}$$

$$y/r = \sin\omega t\cos\alpha_2 + \cos\omega t\sin\alpha_2 \tag{C-4}$$

The following manipulations are then required to eliminate time from these two equations:

1. Multiply equation (C-3) by $\sin\alpha_2$ and equation (C-4) by $\sin\alpha_1$.

2. Subtract the modified equation (C-4) from the modified equation (C-3).

3. Square the resultant equation.

4. Multiply equation (C-3) by $\cos\alpha_2$ and equation (C-4) by $\cos\alpha_1$.

5. Subtract the modified equation (C-4) from modified equation (C-3).

6. Square the resultant equation.

7. Add the equation obtained by step 3 to the equation obtained by step 6.

By judicious use of the trigonometric identity

$$\sin^2\theta + \cos^2\theta \equiv , 1 \tag{C-5}$$

the equation resulting from step 7 becomes

$$\frac{x^2 + y^2 - 2xy\cos(\alpha_2 - \alpha_1)}{r^2 \sin^2(\alpha_2 - \alpha_1)} = 1 \qquad \text{(C-6)}$$

This equation may be shown to be that of an ellipse with the major axis inclined 45° to the x axis. Starting with the equation for an ellipse with the major axis along the x axis

$$x^2/a^2 + y^2/b^2 = 1 \qquad \text{(C-7)}$$

where a and b are the lengths of the major and minor axes, respectively. The following rotational transformation will generate the equation of a 45° inclined ellipse

$$\begin{aligned} x' &= x - y \\ y' &= x + y \end{aligned} \qquad \text{(C-8)}$$

resulting in (dropping the prime sign)

$$(x+y)^2/a^2 + (x-y)^2/b^2 = 2 \qquad \text{(C-9)}$$

as the equation for a 45° inclined ellipse. Comparing this to equation (C-6) it may easily be shown that

$$a^2 = (\sin^2(\alpha_2 - \alpha_1) r^2)/(1 - \cos(\alpha_2 - \alpha_1)) \qquad \text{(C-10)}$$

$$b^2 = (\sin^2(\alpha_2 - \alpha_1) r^2)/(1 + \cos(\alpha_2 - \alpha_1)) \qquad \text{(C-11)}$$

so that, dividing equation (C-11) by equation (C-10) and solving for $\cos(\alpha_2 - \alpha_1)$, we obtain

$$\cos(\alpha_2 - \alpha_1) = (1-(b/a)^2)/(1+(b/a)^2) \qquad \text{(C-12)}$$

Thus, to measure the phase difference between the x and y deflections where they are of the same amplitude, measure the minor and major axes of the generated ellipse and substitute into equation (C-12).

APPENDIX D
TRACE OF B/H CHARACTERISTIC

The emf generated in L_2 of figure 2 of the text is, by Faraday's law of induction, given by

$$e_2(t) = K d\varphi/dt \qquad \text{(D-1)}$$

where K is a constant and φ is the total flux of B through the coil, i.e.,

$$\varphi = \int BdA \qquad \text{(D-2)}$$

Hence, if we subject e_2 to integration via the simple RC integrating circuit shown, we obtain the following for the vertical deflection of the oscilloscope

$$y(t) = K'\varphi(t) \qquad \text{(D-3)}$$

If we assume that the primary L_1 generates a constant magnetic field across L_2 that is proportional to the primary current, then

$$x(t) = K"H(t) \qquad \text{(D-4)}$$

where K" is another proportionality constant. Eliminating the time t between equations (D-3) and (D-4) will result in the following relationship between the x and y deflections

$$B.dA = G(H)$$

If B is constant across the area, this reduces to

$$B = \frac{G(H)}{A}$$

which is the B/H characteristic of interest aside from a scale factor. In fact, H is not constant across L_2 and for certain instances, neither is B, if material properties vary with radial distance from the surface. To this extent, the circuit shown will only give a sort of average B/H characteristic.

APPENDIX E
CALCULATION OF f_g

REFERENCES

(a) McMaster, R. C., et; New York, Vol. II, The Ronald Press Co., (1963)

(b) Foerster, F., Z. Metallkde, Vol. 45, p. 182 (1954)

By definition (references (a) and (b)), f_g is given by the following expression for a cylindrical specimen

$$f_g = 5066/(\mu\sigma d^2) \text{ Hz} \qquad \text{(E-1)}$$

where the units of the variables are

μ = relative permeability, dimensionless

σ = electrical conductivity, meter/ohm-mm^2

d = diameter of cylinder, cm

Based on the measurements made, the following values were used to compute f_g:

$\mu = 47$

$\sigma = 3.5$ meters/ohm-mm^2

d = 1.2 cm

These result in a value of 21 Hz. The basis for each of the above will now be presented.

The value of μ is approximately the same as reported elsewhere for similar steels and is based on the change in inductance of coil L_1 at low frequencies. The value of σ is based on a Kelvin bridge measurement of specimen resistance. At low frequencies $\mu_{eff.r}$ approaches unity so that

$$L = L_o\ (1-\eta+\eta\mu) \qquad \text{(E-2)}$$

the inductance of L_1 devoid of a specimen was measured as being 0.093 henry, while for a multilayer coil of the dimensions of L_1 the average value of η was calculated to be $\eta = 0.23$. Based on these and the measured value of inductance at 5 Hz after insertion of the specimen, the value of μ was calculated from equation (E-2).

APPENDIX F
CALCULATION OF $\Delta\mu/\mu$ FROM HIGH-FREQUENCY MEASUREMENTS

To relate $\Delta\mu_{eff.i}/\mu_{eff.i}$ to $\Delta\mu/\mu$, as is required if we wish to use equation (10) of the text, we first go to equation (13) from which it is easily seen that

$$f' = f/f_g = \frac{\mu\sigma\, d^2\, f}{5066} \qquad \text{(F-1)}$$

Consequently,

$$\Delta f'/f' = \Delta\mu/\mu \qquad \text{(F-2)}$$

From a graphical plot of table 1 of the text, we may numerically derive the quantity n defined as

$$n = (\Delta\mu_{eff.i}/\Delta f') \times (f'/\mu_{eff.i}) \qquad \text{(F-3)}$$

for each f' by estimating the slope at each f'. From equation (F-2) it is also seen that, by substituting in equation (F-3),

$$n = (\Delta\mu_{eff.i}/\mu_{eff.i})/\Delta\mu/\mu \qquad \text{(F-4)}$$

so that

$$\Delta\mu_{eff.i}/\mu_{eff.i} = n \times (\Delta\mu/\mu) \qquad \text{(F-5)}$$

and from equation (15) of the text,

$$R'/R' = (1+n) \times (\Delta\mu/\mu) \qquad \text{(F-6)}$$

Note that n is a negative number.

To complete the basis for this analysis, n has been computed for the frequencies of interest from equation (F-3) and table 1 of the text. These are summarized in table 1-F for the higher frequencies of interest.

TABLE 1-F
TABULATION OF n FOR PLASTICALLY DEFORMED
4130 STEEL SPECIMENS

Frequency khz	f/f_g	$\mu_{eff.i}$	$f'/\mu_{eff.i}$	$\frac{\Delta\mu_{eff.i}}{\Delta f'}$	$\lvert n \rvert$	S mm
10.	500	0.0664	7,500	7.2×10^{-5}	0.54	0.416
20.	1,000	0.0447	21,300	2.4×10^{-5}	0.51	0.23
50.	2,500	0.0421	59,200	4×10^{-6}	0.24	0.146
70.	3,500	0.0387	90,500	$<4\times10^{-6}$	0.2	0.136

APPENDIX G
LOW FREQUENCY CALCULATION OF $\nabla\mu/\mu$

For the specimens under consideration, $f/f_g = 0.25$ at 5 Hz. This is based on the computed value of f_g given in appendix E. For this value of f/f_g it is seen from figure 1 or table 1 of the text, that $\mu_{eff.i} \approx 1$, so that equation (14a) of the text reduces to

$$L = L_o\ (1 - \eta + \eta\mu) \qquad \text{(G-1)}$$

From this equation it is seen that

$$\Delta L/L = \eta\Delta\mu/(1-\eta+\eta\mu) = (\Delta\mu/\mu)/(1+(1-\eta)/\eta\mu) \qquad \text{(G-2)}$$

Substituting the numerical values used previously for η and μ we obtain

$$\Delta u/u = 1.07\ (\Delta L/L) \qquad \text{(G-3)}$$

INITIAL DISTRIBUTION

Copies		CENTER DISTRIBUTION Copies	Code
2	ONR	2	012*
	1 (Code 471)	2	17
	1 (Code 465)	1	28
		1	280
4	NAVSEA	15	2802
	1 (SEA 03C)	2	281
	1 (SEA 035)	6	282
	2 (SEA 09G32)	1	522.1
		2	5231
12	DDC		

*Addressee